Oxidation of Metals (2019) 92:109–121
https://doi.org/10.1007/s11085-019-09916-y

ORIGINAL PAPER

Influence of Temperature on the Oxidation Behaviour of an Austenitic Stainless FeMnSiCrNi Shape Memory Alloy

Yuqin Jiao[1] · Hongxin Zhang[1] · Yuhua Wen[2]

Received: 17 September 2018 / Published online: 17 May 2019

Abstract

The oxidation behaviour of an austenitic stainless Fe–14.29Mn–5.57Si–8.23Cr–4.96Ni (wt%) shape memory alloy was investigated in air at 600 °C and 700 °C. The results showed that the oxidation process obeyed the parabolic rate law at both temperatures. At 700 °C, the final oxide scales were composed of an outer Mn_2O_3 layer, a middle Mn_3O_4 layer, and an inner $MnCr_2O_4$ layer. The scale consisted of only Mn_2O_3 at 600 °C. A composite structure of ferrite and austenite phases was obtained after oxidation at 600 °C and 700 °C because an oxidation-induced Mn-depleted layer formed.

Keywords FeMnSiCrNi shape memory alloys · Oxidation · Mn-depleted layer · Ferrite layer

Introduction

High-manganese FeMnSiCrNi austenitic stainless steel shape memory alloys (SMAs) have attracted considerable attention in the past decade as possible substitutes for expensive Ti–Ni-based SMAs because of their low cost, good workability, machinability, and corrosion-resistant performance [1–10]. However, the Si content in these alloys is 4–6 wt%, which is much higher than that in conventional austenitic stainless steels. Paúl et al. [11] showed that the addition of 0.8% Si enhanced the oxidation resistance of AISI 304 at 1000 °C via the formation of protective SiO_2 films. Adachi et al. [12] showed that the oxidation rate of iron decreased by more than two orders of magnitude with the addition of 5% Si due to the formation of a SiO_2 film. When Si addition is greater than 10%, the oxidation rate of iron is even lower than that of Fe-26Cr, a typical Cr_2O_3-forming alloy [10]. Therefore,

✉ Yuhua Wen
wenyh@scu.edu.cn

[1] School of Mechanical and Electrical Engineering, Qingdao University, Qingdao 266071, China

[2] College of Manufacturing Science and Engineering, Sichuan University, Chengdu 610065, China

investigating the high-temperature oxidation behaviour of austenitic stainless high-manganese FeMnSiCrNi SMAs containing 4–6 wt% Si is important.

In a previous study, we investigated the oxidation behaviour of an Fe14.29Mn5.57Si8.23Cr4.96Ni alloy at 800 °C in air [13]. Although its oxidation behaviour obeyed parabolic law, its weight gain (2.88 mg/cm^2) was much higher than that of 304 stainless steel (0.23 mg/cm^2). However, oxidation remarkably weakens as the temperature decreases. At the same time, the Thermo-Calc® and TCFE7 database confirm that ferrites and G phases precipitate at 700 °C and 600 °C. Therefore, investigating the oxidation behaviour of FeMnSiCrNi SMAs at 700 °C and 600 °C is important. In the present work, the oxidation behaviours of Fe14.29Mn5.57Si8.23Cr4.96Ni alloy at 700 °C and 600 °C in air were investigated and compared with the oxidation behaviour at 800 °C.

Materials and Methods

The experimental alloy was prepared by induction melting under an argon atmosphere using commercially pure iron, manganese, silicon, chromium, and nickel. The chemical composition of the experimental alloy was as follows: 14.29% Mn, 5.57% Si, 8.23% Cr, 4.96% Ni, and balance Fe. After homogenization at 1100 °C for 15 h, the ingot was hot forged at 1100 °C into round bars 15 mm in diameter, and then, the bars were annealed at 1000 °C for 1 h, followed by quenching with water. Finally, the quenched bars were machined to specimens with a diameter of 13 mm and height of 5 mm. Before oxidation, the specimens were mechanically polished using 500-grit SiC paper and then cleaned in ethanol by an ultrasonic bath before the oxidation tests.

The oxidation tests were conducted for different periods in static air at 700 °C and 600 °C. The specimens were placed in individual annealed alumina crucibles with lids to collect the spalled oxide. After various periods of oxidation, the alumina crucibles and specimens were removed from the furnace and air-cooled to room temperature. The mass changes were measured using an electronic balance with an accuracy of 0.1 mg. Three replicates were used in the oxidation assays; each of the data was an average value.

The microstructures were analysed using an optical microscope (OM) and an FEI Inspect scanning electron microscope (SEM) equipped with an energy-dispersive spectrometer (EDS). The cross-sectional specimens were prepared by mounting the specimens in an epoxy mould. After mechanical polishing, the specimens were etched in a solution containing 1 g trinitrophenol, 1 mL hydrochloric acid, and 50 mL ethanol. The above etched specimens were further etched in a solution composed of 1.2 g $K_2S_2O_5$, 0.5 g NH_4HF_2, and 100 mL distilled water to clearly distinguish the phases, which were determined using a Philips X′ Pert Pro MPD X-ray diffraction (XRD) apparatus with a Cu target. The surfaces of the oxidized specimens were also observed by SEM with EDS. The surfaces were ground to characterize the phases present at different depths. A micrometre was used to determine the thickness of the surface removed. A grazing angle X-ray diffractometer (GAXRD) was used to identify the phases of the oxide layer with a 0.02°2θ/step scanning rate at a grazing

angle of 2°. To decrease the influence of the ε martensite phase due to grinding, the mechanically ground specimens were etched in a solution of 5 mL hydrofluoric acid, 25 mL hydrogen peroxide, and 100 mL distilled water.

Results

Figure 1a shows the cyclic oxidation data at different temperatures in air. The measured weight gains were 0.36 mg/cm^2, 1.44 mg/cm^2, and 2.88 mg/cm^2 after oxidation at 600 °C, 700 °C, and 800 °C for 100 h, respectively. A very good positive linear relationship existed between the square of the weight gain and time (Fig. 1b), indicating that the oxidation behaviours of the alloy obeyed a parabolic law at 800 °C, 700 °C, and 600 °C. The corresponding calculated parabolic rate constants were 0.112 mg^2/(cm^4·h), 0.019 mg^2/(cm^4 h), and 1.39×10^{-3}mg^2/(cm^4 h), respectively.

Figure 2 shows the SEM images of the surface after oxidation for 100 h at different temperatures. The oxide scales on the surface of the specimen oxidized at 700 °C were non-compact, directional ridges arranged in strips (Fig. 2a), with a composition of 63.76%Mn, 6.67%Cr, and 29.57%O. In addition, no spallation appeared, but pores and cracks were clearly observed on the oxide scale. The enlarged oxide scales consisted of many nanoparticles. The oxide scales on the surface of the specimen oxidized at 600 °C were arranged in a directional streak (Fig. 2b) and contained 58.60%Mn, 9.14%Cr, and 32.26%O. In addition, some spalled areas consisting of many fuzzy shapes were observed. The composition of these areas was 38.78%Mn, 1.52%Si, 10.52%Cr, 19.25%Fe, 0.31%Ni, and 29.62%O.

Figure 3 shows the cross-sectional OM micrographs of the specimens oxidized for different periods. Regardless of the oxidation temperature, one distinct layer was present between the matrix and the oxidation layer in all the oxidized specimens, and the thicknesses of the layer increased with the increasing oxidation time (Fig. 4). Note that the thickness after oxidation at 800 °C was significantly larger

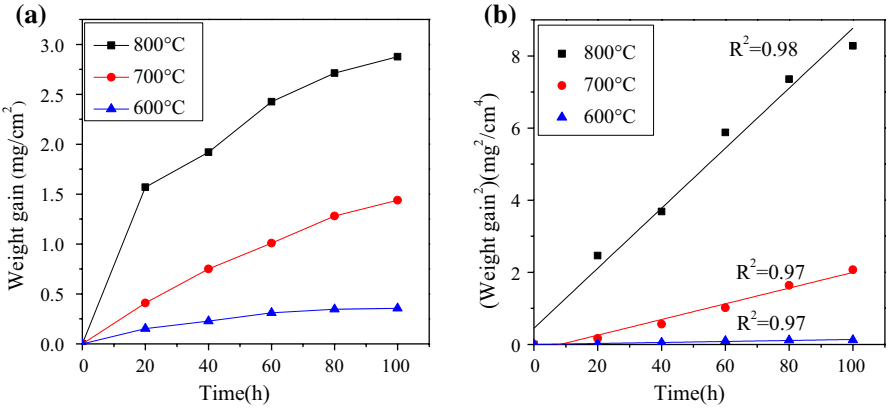

Fig. 1 Weight gain curves (**a**) and square of the weight gain curves (**b**) of alloys oxidized at different temperatures in air. The data at 800 °C were reproduced from the literature [13]

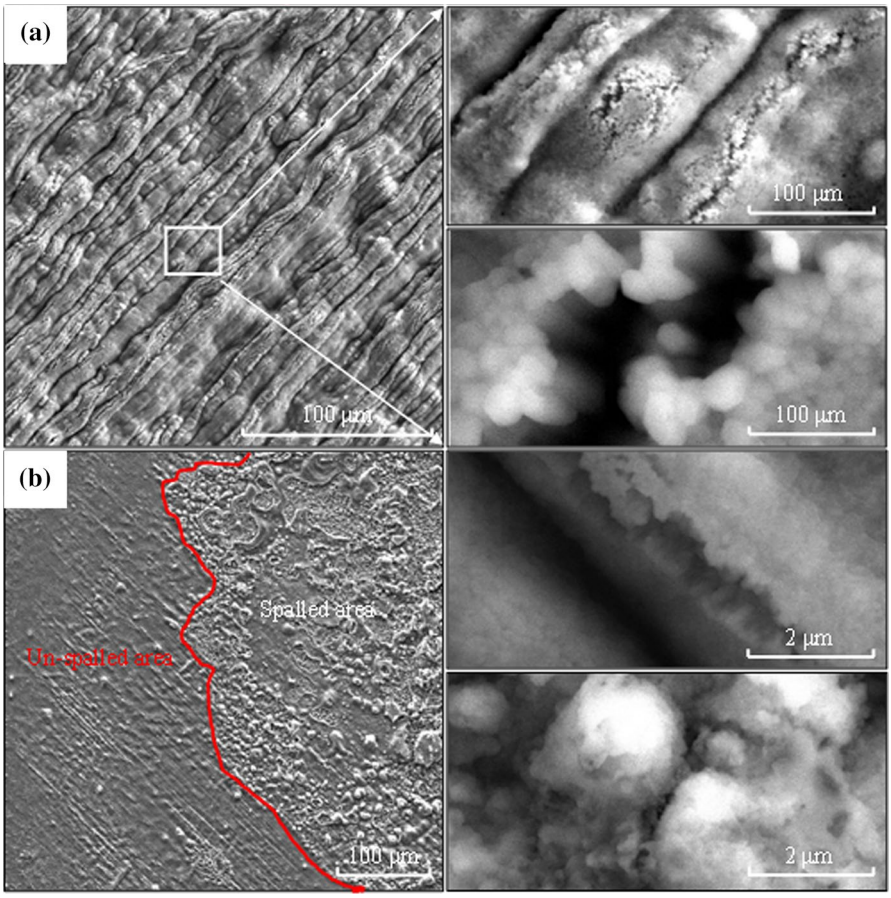

Fig. 2 SEM surface images after 100 h of oxidation at different temperatures in air. **a** 700 °C and **b** 600 °C

than that after oxidation at 700 °C and 600 °C. The XRD results (Fig. 5) revealed that this layer was ferrite, with some chi (χ) phase.

Figures 6 and 7 show the cross-sectional SEM images of the specimens after 100 h of oxidation at 700 °C and 600 °C. The oxide scale well adhered to the ferrite layer. The interfaces between the oxide and ferrite were very irregular. The EDS analysis reveals that the Mn content in the ferrite layer was much lower than the average content in the specimen, i.e. 14.29% (Tables 1, 2). The second-phase particles that precipitated inside the ferrite layer were depleted in Mn but enriched in Si and Ni, while the particles inside the grain boundaries of the matrix were enriched in Mn and Si. These second-phase particles were similar to those obtained after oxidation at 800 °C [13].

The XRD patterns of the specimen surfaces after oxidation at 700 °C and 600 °C for different periods are shown in Fig. 8. After 100 h oxidation, the dominant oxide

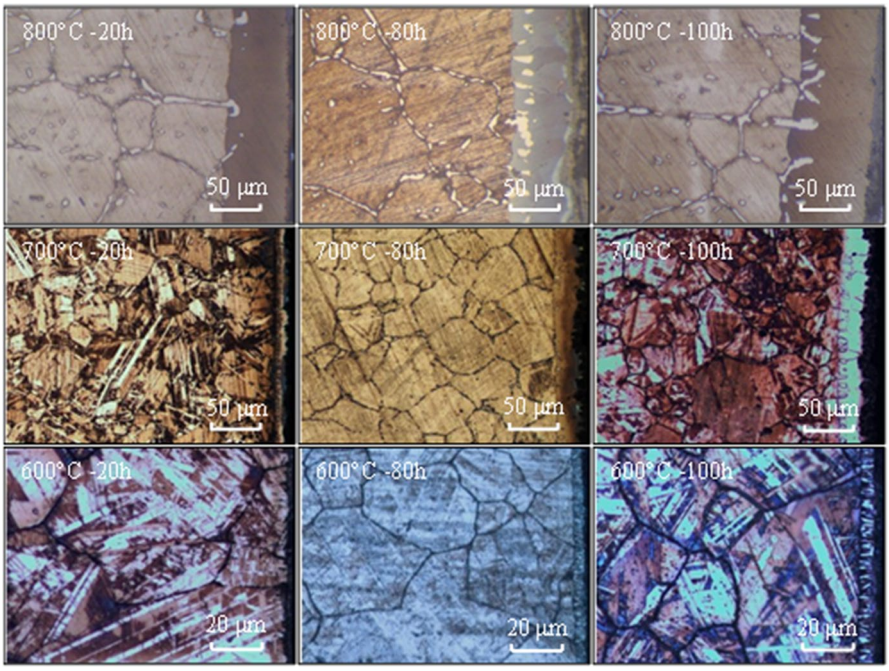

Fig. 3 Cross-sectional optical microstructures of specimens with various exposure times at different temperatures in air

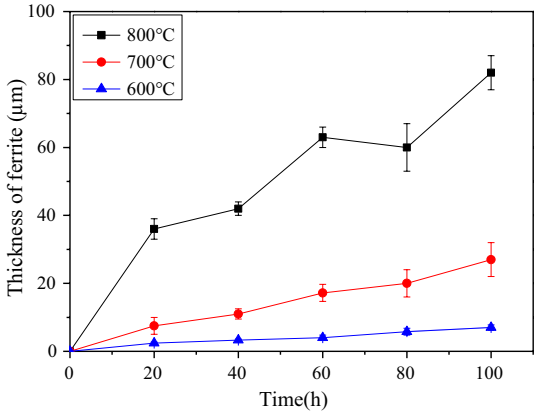

Fig. 4 Effect of the oxidation time at different temperatures on the thickness of the ferrite layer

for both 700 °C and 600 °C was Mn_2O_3. The XRD patterns (Fig. 9) show that the precipitates inside the matrix after oxidation for 100 h at both 700 °C and 600 °C were chi (χ) phases [14].

The surfaces of different specimens oxidized at 700 °C were ground to remove the Mn_2O_3 layer to characterize the oxide scale and ferrite layer. The XRD patterns (Fig. 10) show that the main oxide inside was Mn_2O_3 scale after 5 h of oxidation

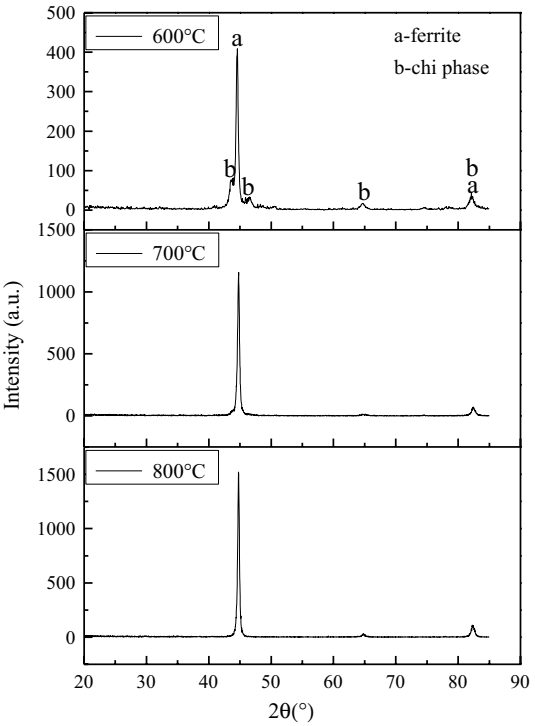

Fig. 5 XRD patterns of the specimens oxidized at different temperatures in air for 100 h after complete removal of the oxide layer

(ICDD-PDF: 04-004-8966). When the oxidation time reached 40 h, several $MnCr_2O_4$ peaks appeared (ICDD-PDF: 00-054-0876), and their intensities increased as the exposure time increased to 100 h, indicating more $MnCr_2O_4$ formed. In addition, many areas with Mn_3O_4 formed close to the $MnCr_2O_4$ (Fig. 10b). In contrast, for oxidization at 600 °C, only Mn_2O_3 peaks were detected in addition to some SiO_2 peaks (Fig. 11).

Discussion

Austenitic stainless steels have been used for chemical processing and energy productions, which both involve exposure to high temperatures ranging from 600 to 900 °C. At these operation temperatures, oxidation resistance is very important and should be considered. Oxidation resistance mainly depends on the oxide scale that forms on the surface. The main oxide scale that forms on conventional austenitic stainless steels is Cr_2O_3 due to their high content of Cr [15, 16]. However, for this tested Fe14.29Mn5.57Si8.23Cr4.96Ni alloy, the outer oxide is Mn_2O_3, the inner oxide is $MnCr_2O_4$, and the middle oxide is Mn_3O_4 at 700 °C and 800 °C [13]. However, the oxide scales that form at 600 °C are different from those that form at 700 °C and 800 °C. At 600 °C, the oxide scale only contains Mn_2O_3. In addition, the oxidation mechanism is also different. The detailed oxidation behaviour at 600 °C is discussed below.

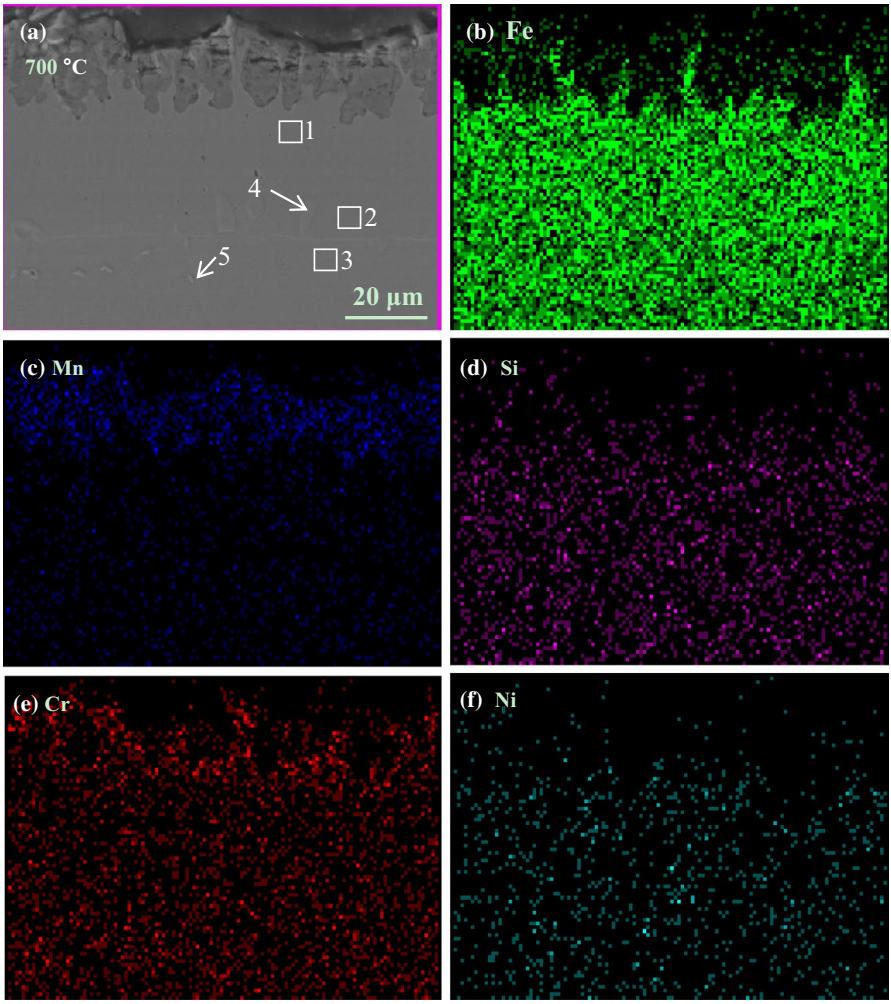

Fig. 6 Elemental mapping of the cross section of the specimen after 100 h of oxidation at 700 °C

Figure 12 shows a schematic diagram of the oxidation behaviour at 600 °C. In the initial oxidation stage, the Mn_2O_3 grains nucleate and grow more quickly within the voids, as shown in Fig. 12b. According to the DSC measurement in Fig. 6 in our previous paper [13], the Mn-depleted layer with compositions of Fe–4.02Mn–6.25Si–8.03Cr–6.5Ni after oxidation at 800 °C for 100 h was austenite at the corresponding oxidation temperature, and it transformed to ferrite during the cooling when the temperature was below 700 °C. For the present Mn-depleted layer with compositions of Fe–3.56Mn–5.86Si–6.92Cr–5.49Ni after oxidation at 600 °C for 100 h, the Mn-depleted layer should be the ferrite at 600 °C.

In this ferrite layer, the diffusion rate of Mn is much higher than that in the austenitic matrix (Fig. 13 and Table 3). Therefore, the subsequent oxidation process

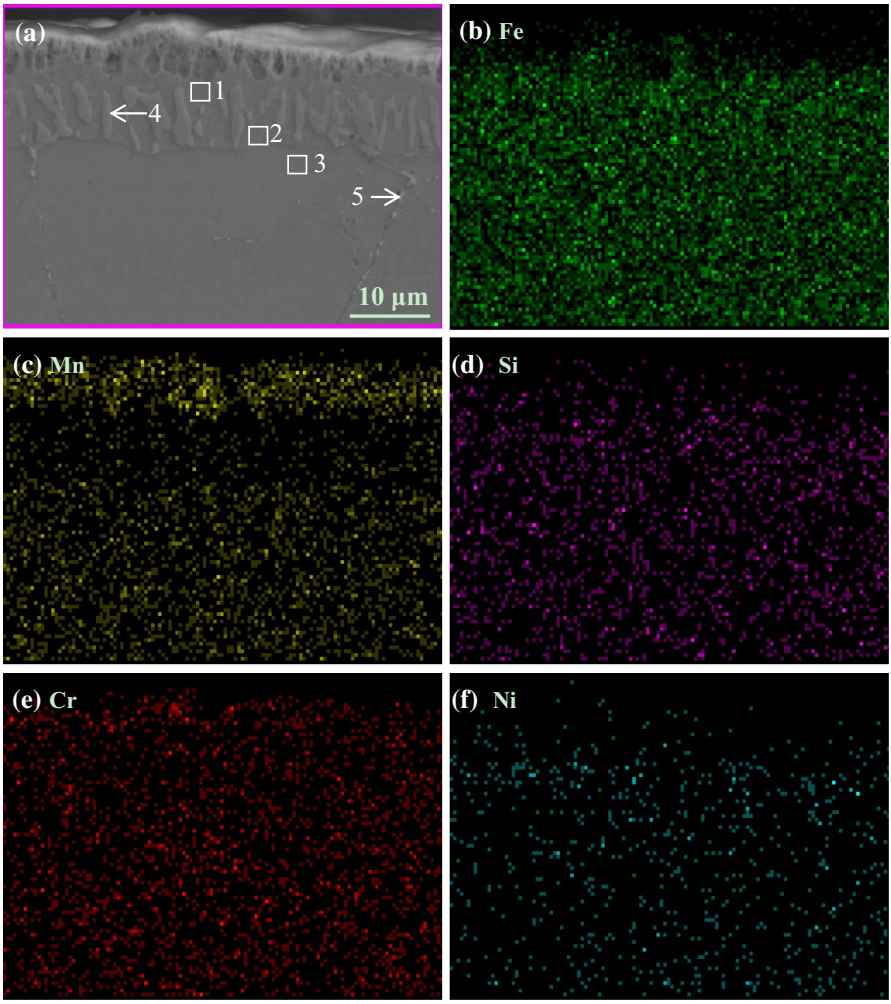

Fig. 7 Elemental mapping of the cross section of the specimen after 100 h of oxidation at 600 °C

Table 1 Micro-area analysis after 100 h of oxidation at 700 °C shown in Fig. 6

Area	Element weight (wt%)				
	Mn	Si	Cr	Ni	Fe
1	1.08	5.79	5.66	5.42	82.05
2	3.56	5.86	6.92	5.49	78.17
3	14.61	4.96	8.50	5.72	66.21
4	4.22	8.86	7.59	11.93	67.40
5	18.44	10.10	9.82	8.65	52.99

Table 2 Micro-area analysis after 100 h of oxidation at 600 °C shown in Fig. 7

Area	Element weight (wt%)				
	Mn	Si	Cr	Ni	Fe
1	1.79	5.48	4.89	3.96	83.88
2	4.94	5.07	6.06	3.85	80.08
3	13.66	5.58	8.37	5.23	67.16
4	7.75	9.73	7.60	12.74	62.18
5	15.07	7.21	10.96	5.26	61.50

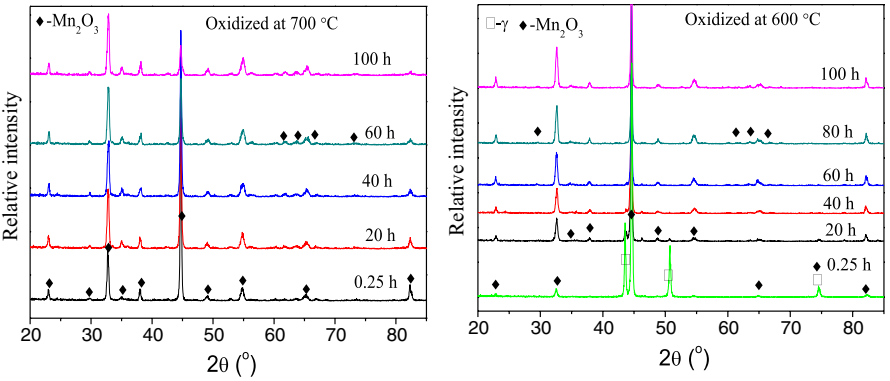

Fig. 8 XRD patterns of the surface of specimens oxidized for 0.25 h, 20 h, 40 h, 60 h, 80 h, and 100 h at different temperatures in air

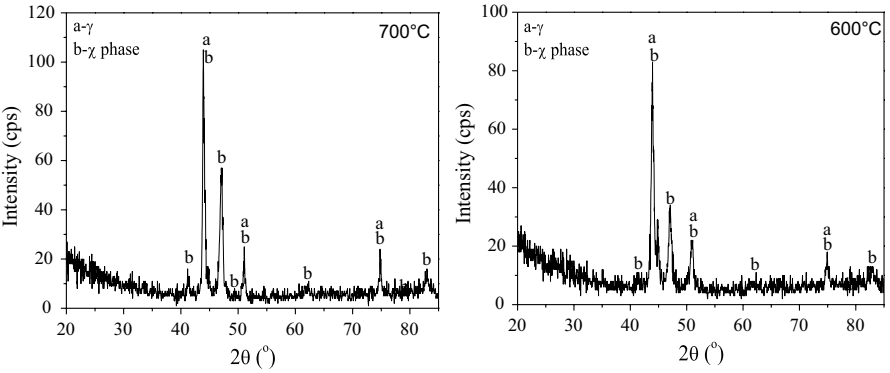

Fig. 9 XRD patterns of the centre area of the cross sections of specimens oxidized for 100 h at different temperatures in air

is controlled by the diffusion of Mn in the matrix. Initially, due to the large concentration gradient, the rapid outward diffusion of Mn increases the thicknesses of the Mn_2O_3 scale and the ferrite layer. As the oxidation time increases, the

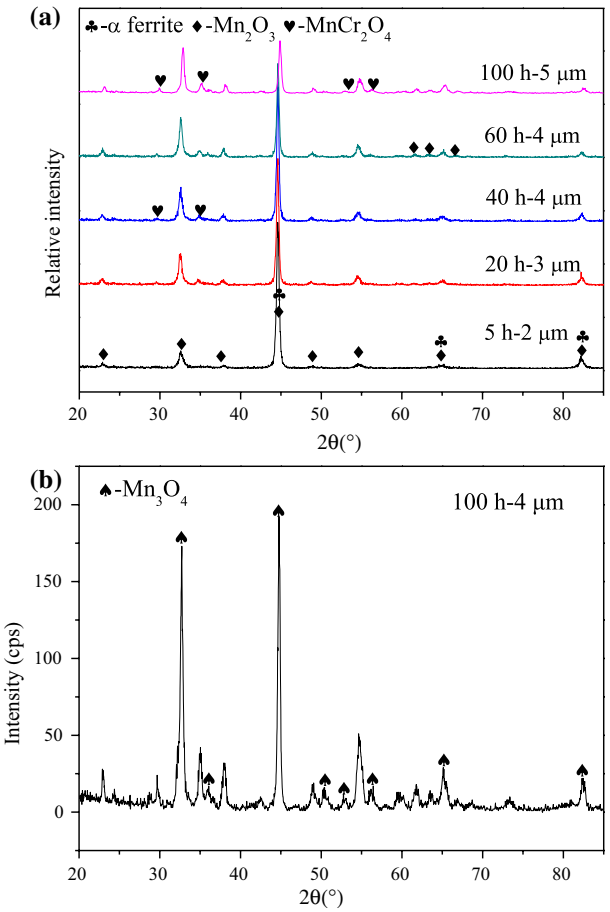

Fig. 10 XRD patterns of the specimens oxidized at 700 °C after removing different surface depths (1 h–1 μm denotes an oxidation time of 1 h and a removed depth of 1 μm)

thickness of the ferrite layer increases, the Mn concentration gradient decreases, and the oxygen partial pressure decreases remarkably. Therefore, the growth rate of the Mn_2O_3 scale decreases. In addition, minimal segregation of Fe, Si, and Cr exists at the interface between the oxide layer and the ferrite layer, and these elements react with oxygen to form their corresponding oxides (Fig. 12d), which is why these elements were detected by the EDS analysis of the spalled areas (Fig. 2).

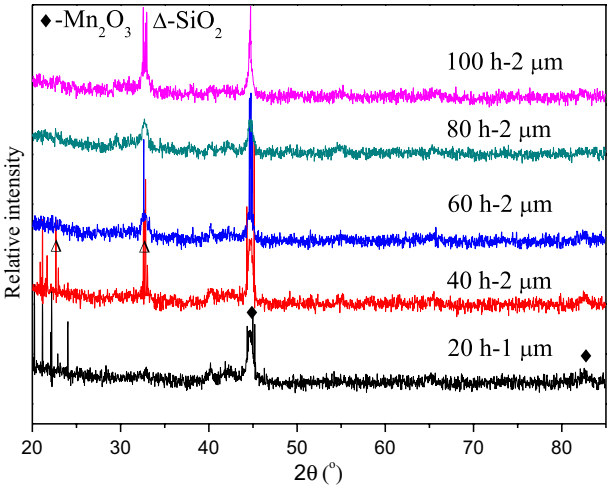

Fig. 11 GAXRD patterns of specimens oxidized at 600 °C after removing different surface depths (1 h–1 μm denotes an oxidation time of 1 h and removed depth of 1 μm)

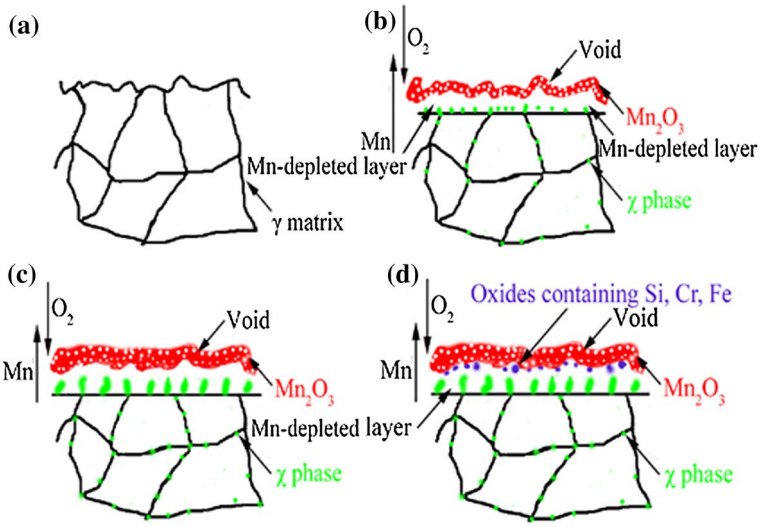

Fig. 12 Schematic illustrations of the oxidation process of FeMnSiCrNi SMAs at 600 °C. **a** Prior to oxidation, the matrix is austenite; **b** in the initial oxidation stage, Mn_2O_3 scale with many voids quickly grows on the surface, resulting in the formation of a Mn-depleted layer, and some chi phase particles precipitate along the grain boundaries and the interface of the matrix and Mn-depleted layer; **c** the amount of Mn_2O_3 scale on the surface increases with increasing oxidation time; **d** eventually, some Si, Cr, and Fe layers form

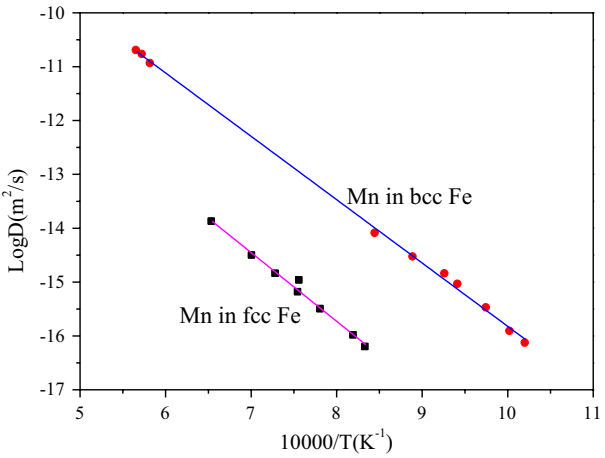

Fig. 13 Relationship between the Mn diffusion rate and temperature in the ferrite and austenitic phases. [17]

Table 3 Diffusion rates of Mn at 600 °C and 700 °C in ferrite and austenitic phases

Temperature (°C)	Diffusivity (cm^2/s)	
	Mn in bcc Fe	Mn in fcc Fe
600	2.95×10^{-14}	7.29×10^{-17}
700	7.16×10^{-13}	2.32×10^{-15}

Conclusions

1. The oxidation behaviour of austenitic Fe–14.29Mn–5.57Si–8.23Cr–4.96Ni shape memory alloy followed a parabolic law at both 600 °C and 700 °C.
2. After 100 h of oxidation at 700 °C, the final oxide scales contained an outer Mn_2O_3 layer, a middle Mn_3O_4 layer, and an inner $MnCr_2O_4$ layer. At 600 °C, only Mn_2O_3 and some SiO_2 were detected.
3. After oxidation at both 600 °C and 700 °C, a relatively large amount of chi (χ) phase precipitated inside the austenite matrix and the ferrite layer.
4. Composite structures containing the ferrite and austenite phases can be obtained after oxidation at 600 °C and 700 °C.

Acknowledgements The authors would like to thank the National Nature Science Foundation of China (No. 51671138) for financial support.

References

1. A. Sato, E. Chishima, K. Soma and T. Mori, *Acta Materialia* **33**, 1982 (1177).
2. H. Otsuka, H. Yamada, T. Maruyama, H. Tanahashi, S. Matsuda and M. Murakami, *ISIJ International* **30**, 1990 (674).
3. N. Bergeon, S. Kajiwara and T. Kikuchi, *Acta Materialia* **48**, 2000 (4053).
4. Y. H. Wen, W. Zhang, N. Li, H. B. Peng and L. R. Xiong, *Acta Materialia* **55**, 2007 (6526–6534).
5. Y. H. Wen, H. B. Peng, P. P. Sun, G. Liu and N. Li, *Scripta Materialia* **62**, 2010 (55–58).
6. H. B. Peng, Y. H. Wen, G. Liu, C. P. Wang and N. Li, *Advanced Engineering Materials* **13**, 2011 (388–394).
7. C. A. D. Rovere, J. H. Alano, R. Silva, P. A. P. Nascente, J. Otubo and S. E. Kuri, *Materials Chemistry and Physics* **133**, 2012 (668–673).
8. C. A. Della Rovere, J. H. Alano, R. Silva, P. A. P. Nascente, J. Otubo and S. E. Kuri, *Corrosion Science* **57**, 2012 (154–161).
9. A. Paúl, S. Elmrabet, L. C. Alves, M. F. da Silva, J. C. Soares and J. A. Odriozola, *Nuclear Instruments and Methods in Physics Research* **181**, 2001 (394–398).
10. T. Adachi and G. H. Meier, *Oxidation of Metals* **27**, 1987 (347–366).
11. F. J. Pérez, M. J. Cristóbal, G. Arnau, M. P. Hierro and J. J. Saura, *Oxidation of Metals* **55**, 2001 (105–118).
12. F. J. Pérez, M. J. Cristóbal and M. P. Hierro, *Oxidation of Metals* **55**, 2001 (165–175).
13. Rui Ma, Huabei Peng, Yuhua Wen, Lijun Zhang and Kai Zhao, *Corrosion Science* **66**, 2013 (269–277).
14. N. Stanford, D. P. Dunne and B. J. Monaghan, *Journal of Alloys and Compounds* **430**, 2007 (107–115).
15. P. J. Maziasz, R. W. Swindeman, J. P. Shingledecker, K. L. More, B. A. Pint, E. Lara-Curzio and N. D. Evans, Proceedings of 6th International Charles Parsons Turbine Conference. in *The Institute of Materials, Minerals, and Mining*, eds. A. Strang, R. D. Conroy, W. M. Banks, M. Blackler, J. Leggett, G. M. McColvin, S. Simpson, M. Smith, F. Starr and R. W. Vanstone (Maney Publishing, London, 2003), pp. 1057–1073.
16. F. J. Pe´rez, M. J. Cristo´bal, G. Arnau, M. P. Hierro and J. J. Saura, *Oxidation of Metals* **55**, 2001 (105–108).
17. Y. J. Liu, L. J. Zhang, Y. Du, et al., *Calphad-Computer Coupling of Phase Diagrams and Thermochemistry* **33**, 2009 (614–623).